

Spectroscopic Study of the Long-Period Dust-Producing WC7pd+O9 Binary HD192641

L. Lefèvre^{1,2*}, S. V. Marchenko³, S. Lépine⁴, A. F. J. Moffat¹, A. Acker²,
T. J. Harries⁵, K. Annuk⁶, D.A. Bohlender⁷, H. Demers¹, Y. Grosdidier⁸,
G. M. Hill⁹, N. D. Morrison¹⁰, D. C. Knauth¹¹, G. Skalkowski¹, S. Viti¹².

¹*Département de Physique, Université de Montréal and Observatoire du mont Mégantic, C.P. 6128, Succ. “Centre-Ville”, Montréal, QC H3C 3J7, Canada.*

²*Observatoire de Strasbourg, Université Louis Pasteur, 11 Rue de l’Université, 67000 Strasbourg, France.*

³*Department of Physics and Astronomy, Western Kentucky University, Bowling Green, KY 42101-3576, USA.*

⁴*Department of Astrophysics, Division of Physical Sciences, American Museum of Natural History, 79th Street, NY 10024, USA.*

⁵*School of Physics, University of Exeter, Stocker Road, Exeter, EX4 4QL, United Kingdom.*

⁶*Tartu Observatory, 61602, Tõravere, Estonia.*

⁷*Herzberg Institute for Astrophysics, National Research Council of Canada, Victoria, BC V9E 2E7, Canada.*

⁸*Ernest Rutherford Physics Building, McGill University, 3600 rue University, Montréal, QC H3A 2T8, Canada.*

⁹*W.M. Keck Observatory, 65-1120 Mamalahoa Highway, Kamuela, HI 96743.*

¹⁰*Ritter Observatory, Dept. of Physics & Astronomy, The University of Toledo, Toledo, OH 43606-3390, USA.*

¹¹*Department of Physics and Astronomy, Northwestern University, Evanston, IL 60208.*

¹²*Department of Physics and Astronomy, University College London, Gower Street, London Wc1E 6BT.*

Accepted 2004 December 15. Received 2004 December 14; in original form 2004 October 11

ABSTRACT

We present the results of an optical spectroscopic study of the massive Wolf-Rayet binary HD192641=WR137. These 1986-2000 data cover the dust-formation maximum in 1997. Combining all available measurements of radial velocities, we derive, for the first time, a spectroscopic orbit with period 4766 ± 66 days (13.05 ± 0.18 years). The resulting masses, adopting $i=67^\circ$, are $M_O=20 \pm 2M_\odot$ for the O component and $M_{WR}=4.4 \pm 1.5M_\odot$ for the WR component. These appear, respectively, \sim normal and on the low side for the given spectral types. Analysis of the intense multi-site spectroscopic monitoring in 1999 shows that the CIII $\lambda 5696$ and CIV $\lambda 5802/12$ lines have the highest intrinsic variability levels. The periodogram analysis yields a small-amplitude modulation in the absorption troughs of the CIV $\lambda 5802/12$ and HeI $\lambda 5876$ lines with a period of 0.83 days, which could be related either to pulsations or large-scale rotating structures as seen in the WN4 star EZ Canis Majoris (WR6). Wavelet analysis of the strong emission lines of CIII $\lambda 5696$ and CIV $\lambda 5802/12$ enabled us to isolate and follow for several hours small structures (emission subpeaks) associated with density enhancements within the wind of the Wolf-Rayet star. Cross-correlating the variability patterns seen in different lines, we find a weak but significant correlation between the variability in emission lines with different ionization potential, i.e. in lines formed at different distances from the WR stellar core. Adopting a β wind-velocity law, from the motion of individual subpeaks we find $\beta \sim 5$, which is significantly larger than the canonical value $\beta \simeq 1$ found in O-star winds.

Key words: stars: Wolf-Rayet - stars: wind, outflows - stars: oscillations - binaries: spectroscopic

* E-mail: lefevre@astro.umontreal.ca, sergey@astro.wku.edu, lepine@amnh.org, moffat,demers, skalkowski@astro.umontreal.ca, acker@astro.u-strasbg.fr, th@astro.ex.ac.uk, annuk@aaai.ee, david.bohlender@nrc-cnrc.gc.ca, gyves@physics.mcgill.ca,

hill@keck.hawaii.edu,

nmorris2@uoft02.utoledo.edu,

dknauth@pha.jhu.edu, sv@star.ucl.ac.uk

1 INTRODUCTION

Population I Wolf-Rayet stars are highly evolved He-burning descendents of massive OB-stars, which are assumed to have undergone rapid luminous blue variable (LBV) mass-loss episodes before reaching the WR stage (Langer et al. 1994). They exhibit intense broad emission lines produced by highly-ionized atoms (Conti 2000), which form a hot, fast and dense stellar wind (Hamann & Koesterke 1998). Furthermore, recent observations (Moffat et al. 1988; Lépine & Moffat 1999; Lépine et al. 2000) revealed that the winds are highly structured, although the “Standard Model” of a WR-star wind was based on the simplifying assumptions of spherical symmetry, homogeneity, time independence and a monotonic velocity law for the wind (Hillier 1991; Hamann 1991). The highly structured nature of the winds may be related to numerous small-scale density enhancements embedded in the outmoving WR wind. Once included in the framework of the “Standard Model”, the micro-structuring (clumping) allowed one to: (i) produce much better fits of the emission line profiles (especially in the red-shifted electron-scattering wings: Hamann & Koesterke 1998), (ii) bring theoretical spectral energy distributions closer to the observed infrared and radio fluxes (Nugis et al. 1998).

There are two broad classes of WR stars: WN, where nitrogen lines dominate, and WC (WO), with dominance of carbon (oxygen). These two classes may then be further divided according to spectral ionisation related to wind temperature. Many of the cooler WC subtypes are known to be prolific dust makers. There are two situations in which a WC star can produce dust: (1) in a presumably single WC star of late spectral subtype (mainly WC9 and some WC8) and (2) in a WC+O binary with a relatively long-period, often eccentric, orbit and no restrictions on the WC subtype. Currently seven WC stars are known to be episodic dust makers with periods or suspected periods of several years. We refer here to WR19 (WC4), WR48a (WC8), WR70 and WR98a (WC9), and three WC7 stars WR125, WR137 and WR140 (Williams 1995). All of these are confirmed or suspected binaries with elliptical orbits and massive companions. They serve as unique laboratories, allowing one to study formation of dust in most hostile environments (Harries et al. 2004; Marchenko et al. 2002, 2003; Monnier et al. 1999, 2002; Tuthill et al. 1999; Williams 2001).

As one of the dust-producing prototypes, WR137 (*WC7pd+O9*, van der Hucht 2001) was frequently observed in the last two decades. The initial discovery that WR137 forms dust during large IR outbursts (Williams et al. 1985) prompted various investigators to obtain observations in 1997-1998 during the most recent outburst. One of these studies based on near-IR HST/NICMOS2 images (around the predicted periastron passage, Marchenko et al. 1999), revealed dust clumps leaving the system. Different IR and UV photometry campaigns yielded a ~ 13 year modulation (Panov et al. 2000; Williams 2001) which was supposed to be related to the presence of a binary. WR 137 also shows a strong polarisation “line effect”, possibly produced in a spatially anisotropic (flattened) wind (Harries et al. 2000). Two of the best studied “line effect” WR systems, WR6 (Harries et al. 1998, 1999) and WR134 (Harries et al. 1998),

reveal the presence of periodically repeatable structures in their winds (Morel et al. 1997, 1999, and references therein). We organised an intense multi-site spectroscopic monitoring campaign of WR137 in 1999-2000 in order to improve the orbital parameters and study the structure of the WR wind and thus obtain a better understanding of the dust formation process. Here we report on the results of this campaign and its integration into previous observations.

2 OBSERVATIONS

Spectroscopic CCD data were obtained from 1986 to 2000 at six different observatories (see Table 1) with 1-2 m class telescopes: the Observatoire de Haute Provence (France), hereafter OHP; the Observatoire du Mont Megantic (Quebec), OMM; the Tartu Observatory (Estonia), TO; the Dominion Astrophysical Observatory (Victoria, Canada), DAO; the Ritter Observatory (Toledo, Ohio), RO; and the Kitt Peak National Observatory (Arizona), KPNO.

3 REDUCTION AND ANALYSIS

All spectra were extracted locally at each observatory using standard routines (mainly de-biasing, flat-fielding and conversion to a one-dimensional spectrum). The remaining calibration steps (wavelength calibration, continuum rectification, removal of the telluric spectrum) were performed for all the spectra in succession using standard IRAF¹ routines, thus producing a homogeneous data set. During the continuum rectification we made sure that all the parameters, especially the wavelength windows assigned to a line-free continuum, were identical for all the spectra, although the much higher resolution but limited spectral range of the KPNO spectra forced us to choose fewer continuum windows (although similar ones for the overlapping range) for their rectification. Spectral samples used for the determination of the continuum are shown in the top panel of Figure 1.

To be able to detect and measure subtle temporal variations in the WR line profiles, we carefully removed the telluric lines from all the spectra. Using normalized spectra of WR 137 taken at different air masses, we created a template of the telluric lines, then divided the appropriately scaled and binned (to attain the same resolution as the target spectrum) template into each observed spectrum. Additional iterative adjustment of the intensities and positions of the telluric lines allowed us to achieve an optimal removal.

3.1 Assessing variations in the spectra

3.1.1 Temporal Variance Spectrum

Observing line profile variability in WR spectra, one may encounter several types of intrinsic variations: a stochastic component related to the small-scale inhomogeneities in the wind (Moffat et al. 1988; Lépine & Moffat 1999),

¹ IRAF is distributed by the National Optical Astronomy Observatories, operated by the Association of Universities for Research in Astronomy, Inc., under cooperative agreement with the National Science Foundation.

Table 1. Summary of Observing Runs.

Site	telescope (m)	UT dates	No. Spectra	Sp. Coverage (Å)	Sp. Dispersion (Å/pix)	S/N (cont.)
DAO	1.8	08/1986-07/1999	41	5300-6100	0.75	250
KPNO	0.9	11-19/09/1999	58	5600-6000	0.10	100
OHP	1.5	01/1997-07/1999	50	5200-6100	0.35	60
OMM	1.6	07/1991-09/1999	55	5100-6600	0.65	80
RO	1.0	06/1999-09/1999	67	5100-6100	1.50	90
TO	1.5	06/1999-03/2000	27	5600-6000	0.80	60
Total			236			

as well as periodic variations on various timescales from hours to weeks, presumably caused either by pulsation, rotation or an orbiting companion (Bratschi & Blecha 1996). To assess whether the variability patterns are intrinsic to the star or due to spurious features introduced during the reduction process (mainly associated with the continuum fitting and wavelength calibration), we use the “Temporal Variance Spectrum” (TVS) approach (Fullerton et al. 1996; Prinja et al. 1996; Marchenko et al. 1998). At each wavelength (index j) we calculate:

$$TVS_j = \frac{1}{N-1} \sum_{i=1}^N \left(\frac{\bar{\sigma}_0}{\sigma_i}\right)^2 \frac{1}{\bar{S}_j} (S_{ij} - \bar{S}_j)^2 - \bar{\sigma}^2 \rho_j^2 \quad (1)$$

where index i refers to a given spectrum (total number N), $\left(\frac{\bar{\sigma}_0}{\sigma_i}\right)^2$ is taken to be 1 ($\bar{\sigma}_0$ is the noise determined for the entire time series and σ_i the noise determined from continuum pixels in each spectrum), S_{ij} is a spectrum taken at time t_i at the j^{th} pixel or wavelength and \bar{S}_j is the spectrum averaged over time (index i). The last term of the equation helps to eliminate the spurious details arising from small positional errors introduced during the wavelength calibration: $\bar{\sigma}$ is proportional to the typical error of the radial velocities, and ρ_j is the gradient of \bar{S}_j with respect to the wavelength.

As defined, the TVS does not provide any detailed information about temporal characteristics of the line profile variability. This can be remedied by calculating TVSs for isolated sub-sets. We have therefore calculated a TVS for each set of observations. We grouped the data sets in different ways to access different variability periods. Data sets were first grouped on a day-by-day basis, showing significant variability of the strong emission lines CIII $\lambda 5696$ and CIV $\lambda 5802/12$. Then the data were grouped in gradually larger intervals. The most representative sub-set for OHP, OMM, DAO, TO data (1999, July) is shown in Figure 1 along with the TVS for the KPNO data (1999, September). The TVS for the RO data is similar in shape but the variations are less significant, as expected from the higher noise level of the data. It is not shown here for reasons of clarity.

Statistical behavior of the TVS follows a $\sigma_0^2 \chi_{N-1}^2$ distribution, hence thresholds (straight lines in our case) of a given statistical significance can be drawn for each TVS: $T = \sigma_0^2 \chi_{N-1}^2$, where N is the number of spectra and σ_0 refers to the noise level in the adjacent continuum. In Figure 1 one can see that the variations in the CIII $\lambda 5696$ and CIV $\lambda 5802/12$ lines are significant at the 99% level (i.e., exceeding the 1% threshold) for the combined OHP, OMM, DAO, TO data.

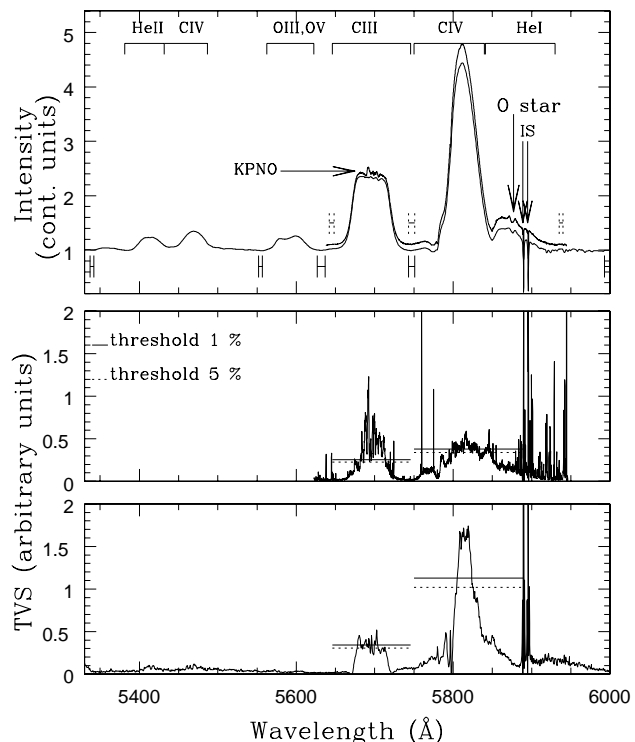


Figure 1. The upper panel shows the reference mean spectrum of WR137 (combined OHP, OMM, DAO, TO and RO data sets) with the superposed, vertically shifted (for clarity) mean spectrum from the KPNO set. The continuum windows used for both sets are displayed in the form of horizontal bars. The upper ones refer to KPNO data while the lower ones refer to OHP, OMM, DAO, TO and RO data. The middle panel shows the TVS for the KPNO data for September 11-19 1999, and the lower panel shows the TVS for the combined July 1999 sets from DAO, OHP, OMM and TO.

It turns out that the observed profile variations (Fig. 1 and other TVSs not shown here) are practically always significant at the 99% level. The spike-like features around the sharp interstellar Na D1/D2 lines at $\lambda 5890/96$ are caused by combinations of spectra with different spectral resolutions (bottom panel) or difficulties in fitting the continuum (middle panel). Indeed, the RO TVS (not shown here) does not display these features as long as it is a combination of data from the same instrument and the continuum is well defined.

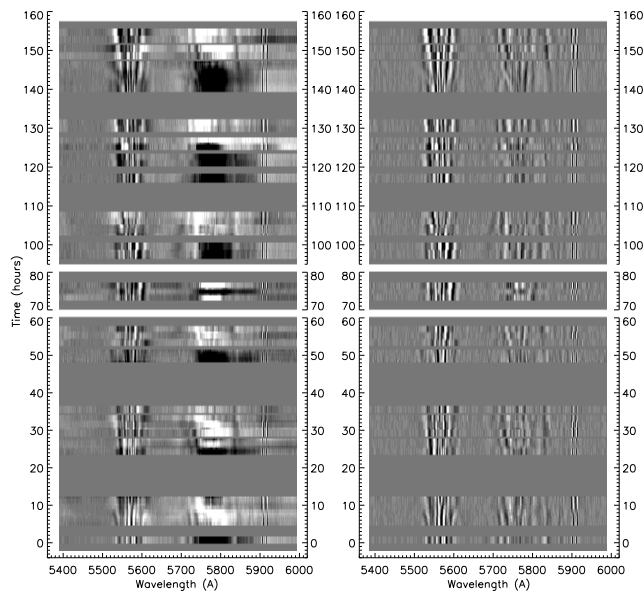


Figure 2. Sequence of residuals of the strongest lines (CIII $\lambda 5696$ and CIV $\lambda 5802/12$) after the average spectrum of the 1999 multi-site run has been subtracted from each individual spectrum. The residuals are displayed as a greyscale plot and stacked sequentially from bottom to top. The white horizontal bands separate spectra obtained on different nights. The grey horizontal bands represent missing spectra. This Figure represents nights from July 21 to 31, 1999, where we have the highest density of data. The average spectrum is shown in Fig.3. The left panel shows the residuals after subtraction, while the right panel shows the same residuals after the large-scale variable components have been filtered out with the power spectrum shown in Figure 3. Note the variability occurring in the form of narrow moving features in the CIII $\lambda 5696$ emission line, and in the form of global line-strength variations in CIV $\lambda 5802/12$ on the left panel. While the former is intrinsic to the star, the latter is an artefact of the spectral rectification. In the right panel, much of the (spurious) global variability in the emission line strengths has been removed, leaving only the signature of the intrinsic narrow moving subpeaks. Variability patterns from the narrow subpeaks are quite obvious in CIII $\lambda 5696$ and CIV $\lambda 5802/12$.

3.1.2 Wavelet analysis

In order to investigate the variability in the different spectral lines on a relatively small scale, it is possible to use the wavelet techniques described in Lépine et al. (2000). To perform this analysis of rapid spectral variations, a carefully computed mean spectrum must be subtracted from the individual spectra.

The mean spectrum was constructed in steps. First, the sub-sets of the data (usually the rectified, telluric-free spectra from the same observatory) were grouped into preliminary means. Then, these groups were cleaned from any deviating spectra (comparing the preliminary mean to the individual spectra), forming the final mean spectra. The final mean spectra at similar spectral resolution (OHP, OMM, DAO, TO) were used to form, via simple averaging, the template mean used in this section. Due

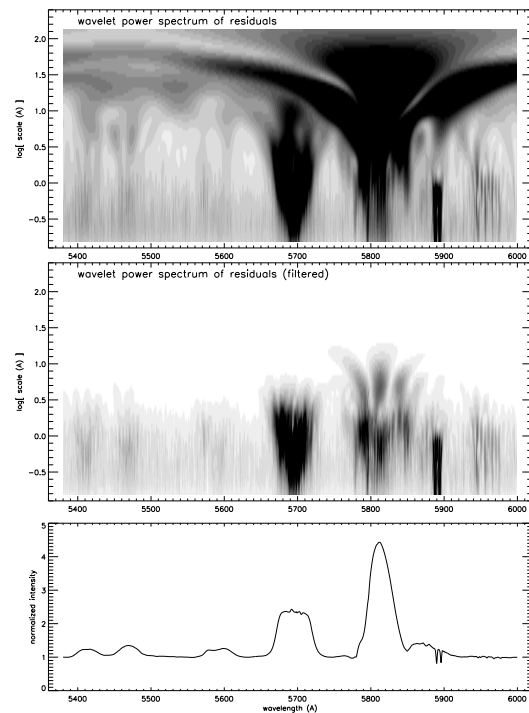


Figure 3. Mean wavelet power spectrum of the residuals (top) and of the wavelet filtered residuals (centre). The residuals yield a strong response at small scales near the CIII $\lambda 5696$ line, and at larger scales near CIV $\lambda 5802/12$, consistent with the variability patterns observed in Figure 2. Filtering out the large-scale (instrumental) components leaves only the signature of the (intrinsic) narrow variable subpeaks. The wavelet power spectrum of the filtered residuals yields a positive identification of narrow emission features in both CIII $\lambda 5696$ and CIV $\lambda 5802/12$, and suggests that narrow variable features are also present in HeII $\lambda 5411$, CIV $\lambda 5471$ and OV $\lambda 5592$ (grey patches).

to the different spectral resolutions, the KPNO and RO data were first treated separately. We show that all the most prominent emission lines in the 5400-6000Å range are variable, predominantly in the form of narrow emission subpeaks moving across the broad line profiles.

In Figure 2 (left) we plot deviations from the average profile (shown at the bottom of Figure 3) for spectra obtained during the 1999 multi-site campaign (OHP, OMM, DAO, TO, RO) for the CIII $\lambda 5696$ and CIV $\lambda 5802/12$ lines and only for the nights where the temporal coverage is the best. Two types of variability patterns are apparent in the residuals: (1) patterns marked by narrow moving features as is most apparent in the CIII $\lambda 5696$ emission line, and (2) broad patterns that suggest that the whole line is globally increasing or decreasing in strength, as is most obvious in the CIV $\lambda\lambda 5802/12$ emission doublet. The first patterns correspond to the moving emission-line features seen in the spectra of many WR stars (Lépine & Moffat 1999). The second pattern, on the other hand, is largely an artefact of the data reduction procedure. All spectra have been rectified to a pseudo-continuum level. The pseudo-continuum is poorly defined in the regions with numerous blended, broad emission features. The chosen pseudo-continuum sampling pro-

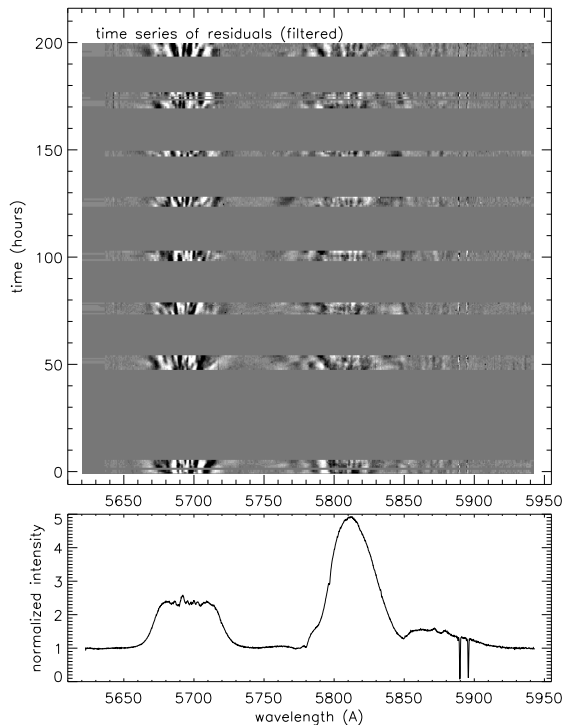


Figure 4. The KPNO run: temporal sequence of residuals after the large-scale variable components have been filtered out - compare to Figure 2.

duces relatively small, but, nevertheless, easily detectable systematic differences between the groups of spectra (usually coming from different observatories).

Fortunately, the variability of the intrinsic narrow moving features and that of the global (spurious) line strength variations have very different characteristic scales. It is thus possible to separate them using wavelet analysis. In Figure 3, we display the mean wavelet power spectrum of the residuals. The narrow Discrete Wind Emission Elements (DWEES; see Lépine & Moffat 1999) introduce a significant response on scales of $\approx 1 \text{ \AA}$. Note the very dark patch near 5700 \AA that is associated with the high-amplitude DWEES in CIII $\lambda 5696$. Global line variations, on the other hand, yield responses over much larger scales. The very large, dark patch near 5800 \AA that extends to scales of several tens of \AA is the signature of the large pseudo-continuum rectification artefact in CIV $\lambda\lambda 5802/12$. Note also the narrow dark patch near 5890 \AA extending over a range of very small scales ($< 1 \text{ \AA}$): this corresponds to another artefact associated with the interstellar absorption doublet. Because the spectra from different observatories have slightly different spectral resolutions, subtraction of the mean profile from the individual spectra introduces residual features that are very apparent in Figure 2.

We use wavelet filtering to remove the rectification artefact from the time series of residuals. Keeping only wavelet coefficients on the smallest scales ($< 4 \text{ \AA}$), we use the wavelet reconstruction theorem to rebuild each individual residual spectrum. The mean wavelet power spectrum of the filtered residuals is displayed in Figure 3. A time series of the filtered residuals is displayed in the right panel of Figure 2, and can

be compared to the original time series in the left panel of the same figure. One sees that all large scale variable features have been filtered out. The narrow moving features in the CIV $\lambda\lambda 5802/12$ emission doublet, which initially were completely drowned out in the (spurious) global line-strength variations are now clearly visible. These intrinsic features are weaker than those in CIII $\lambda 5696$. This behavior mimics the variability patterns seen in emission lines of the single WC8 star WR135 (Lépine et al. 2000).

A thorough examination of the filtered residuals and corresponding wavelet power spectrum also reveals what appears to be a very weak signature from intrinsic narrow emission features in the three prominent emission lines bluewards of CIII $\lambda 5696$. In Figure 3, darker patches can be seen matching the locations of HeII $\lambda 5411$, CIV $\lambda 5471$ and OV $\lambda 5592$, indicating a significant component of variable features at the scale expected for the narrow emission-line subpeaks.

The same wavelet-filtering procedure is repeated for the spectroscopic time-series obtained during the Kitt-Peak run. Again, random variations on large scales affect the CIV $\lambda\lambda 5802/12$ doublet, and these are an artefact of the spectral rectification. Fortunately, these artefacts occur on a scale ($> 10 \text{ \AA}$) that is larger than that of the intrinsic DWEES, and they are easily filtered out. The resolution of the Kitt-Peak spectra (0.1 \AA per pixel) is higher than that of the other sub-sets of data, hence one may obtain a clearer picture of the scale properties of the DWEES. The behavior is largely the same as noticed by Lépine & Moffat (1999), producing, in the wavelet power diagram, the shape of a symmetric triangle standing on its tip which marks the centre of the emission line, where the DWEES are narrower than near the edges of the line. The time-series of the wavelet-filtered KPNO spectra is shown in Figure 4. The general motion of the DWEES, from the line centre toward the line edges, is quite apparent in CIII $\lambda 5696$ and CIV $\lambda\lambda 5802/12$, thus confirming the presence of a strong variability as seen in the TVS analysis in section 3.1.1. From the KPNO time-series, as for the previous one, the DWEES in CIII $\lambda 5696$, if compared to CIV $\lambda\lambda 5802/12$, do not give the impression that they follow similar patterns. However, the doublet nature of the CIV transition may confuse things considerably. Hence, we must explore the possibility that the variability in the different emission lines follows similar patterns. Such behavior would be consistent with a model of the wind where the different emission lines are formed at different depths in the wind on average, depending on their excitation potential, but with a significant overlap between the emission regions (Herald et al. 2000). Therefore, line profile variations caused by outmoving clumps would be expected to show up in all the lines at similar times (Lépine 1996; Lépine et al. 2000). This will be discussed in detail in section 3.2.2.

3.1.3 Periodograms

Inspired by the positive results of the TVS analysis, we also searched the spectra for periods using the periodogram approach of Scargle (1982) combined with the cleaning algorithm of Roberts et al. (1987). Following Scargle (1982), we use $N_0 = N/2$ frequencies ω , noting that the number of observations, N , could be different for the TVS and periodogram samples. This defines the corresponding false alarm probability thresholds: $T \approx \ln(N_0/p_0)$, where

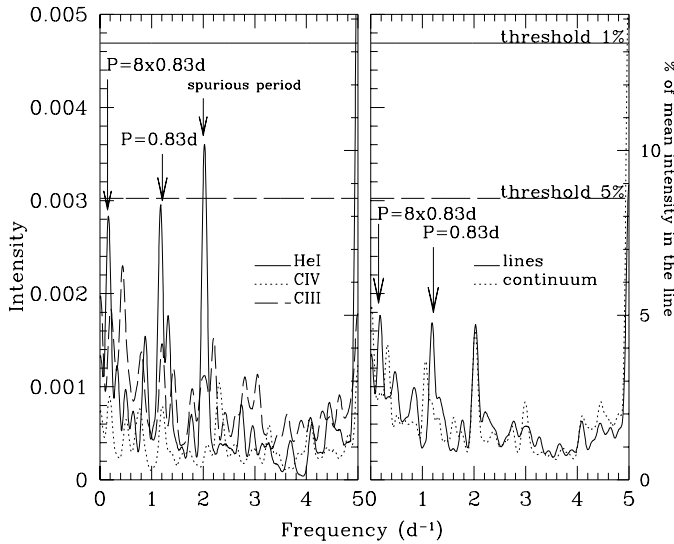


Figure 5. Kitt Peak Observatory periodograms reduced to one dimension. The average periodograms for the P Cygni absorption part of the three main lines (CIII at 5670-5692, CIV at 5755-5776 and HeI at 5838-5848) are shown in the left panel while the average periodograms of the two main lines (CIII at 5670-5720 and CIV at 5785-5835) along with the continuum (λ 5645-5665, 5735-5755, 5900-5930) are shown in the right panel. The false alarm probability threshold levels are also indicated.

p_0 is the false-alarm probability, usually set at 0.01-0.05. The cleaning procedure effectively suppresses the false periodicities arising from the non-regular character of the observations, the most prominent ones coming from the daily sampling bias of the data sets (see Fig. 5). Although we found no periodic behavior in the spectra from OHP, DAO, TO, RO or OMM, this method yielded a small-amplitude, 0.83 ± 0.04 -day period in the KPNO spectra, searching in the range $P=0.2$ -30d. Probably, both the high homogeneity of this particular set, as well as its high spectral resolution helped to detect the low-amplitude signal.

We use wavelet filtering to isolate two different components of the variability: *small-scale* ($\leq 4 \text{ \AA}$) and *large-scale* ($> 4 \text{ \AA}$) structures (methods described in section 3.1.2) in order to distinguish between real variability and artefacts of the spectral rectification. The presence of this 0.83d period in the *large-scale structures* (i.e. associated with overall variations of the continuum caused by errors in its fit) would invalidate its existence while its appearance in the *small-scale structures* would suggest that it is real.

We found no significant signals in the *wavelet filtered* (either small- or large-scale) periodograms calculated from averaged fluxes of the emission parts of the three major lines: CIII (5670-5720 domain), CIV (5785-5835) and HeI (5865-5885). On the other hand, the periodogram of the P Cygni absorption parts shows a clear peak at 0.83d for CIII while the peaks are diminished for the CIV and HeI lines. Moreover, the 0.83d signal is absent from the *large scale structures* in the CIV, CIII and HeI lines of the same periodogram. Combining the results from Fig.5 and the wavelet filtered periodograms, we conclude that: (1) there is no periodic sig-

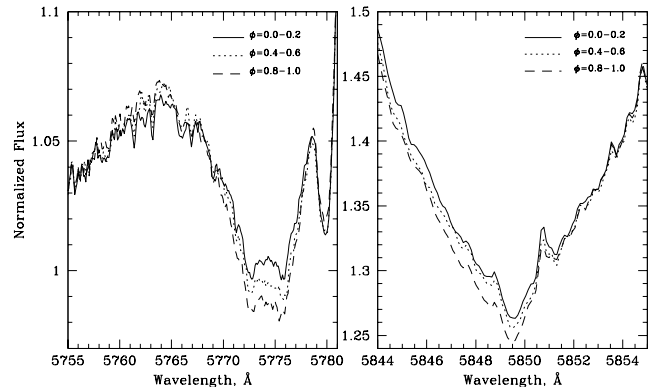


Figure 6. Absorption troughs of CIV λ 5802/12 (left) and HeI λ 5876 (right) phased ($P=0.83$ d, T_0 =HJD 2480198) with the 0.83d period found exclusively in the KPNO data. Different lines depict average profiles calculated for the given phase bins.

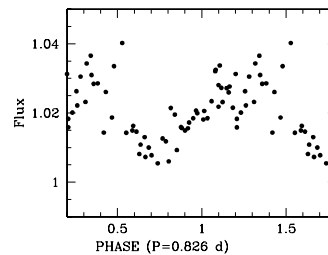


Figure 7. Averaged flux in the 5750-5780 \AA range of the CIV λ 5802/12 line versus phase ($P=0.83$ d; $T_0=2450198$ d) for the KPNO data.

nal in the emission parts as suggested by the wavelet filtered periodograms of the lines; (2) there is a periodic signal at 0.83d, but it can be seen **only** in the small-scale structures in CIII λ 5696 (it is amplified by the filtering) and in the absorption part of HeI λ 5876 (Fig. 5, left panel). Note that, though the unfiltered signal in CIII λ 5696 falls much below statistically significant levels, wavelet filtering allows one to increase the period's visibility rather dramatically. This different behaviour of the CIII line is to be expected as it has no discernible P Cygni trough, and all the variability seems to be concentrated there. It is no surprise either to find no 0.83d signal in the CIII line in the unfiltered data: this signal shows only in the filtered *small-scale* set, being restricted to the blue wing of the CIII line profile, roughly located at the same place as the CIV and HeII counterparts.

We show the phase-binned profiles of CIV and HeI in Fig.6 and an average flux coming from the P Cygni absorption trough of CIV in Fig. 7. Both the amplitude (0.5%-1.5% of the continuum) and period of this variation are small compared to similar cases as seen for two other single WR stars with similar large-scale periodic spectral variations (WR134 and WR6), where the amplitude is 5%-10% of the continuum and the periods are 2.31d and 3.76d, respectively (Morel et al. 1997, 1999). Note that, by themselves, the significance levels plotted in Figure 5 are uncomfortably low. This may be related to the relatively high level of the noise introduced by the adopted procedure of rectification: note that, while calculating the respective values, we used the unfiltered KPNO spectra. However, Figures 6 and 7 lend strong support to the 0.83-day periodicity. Note that these

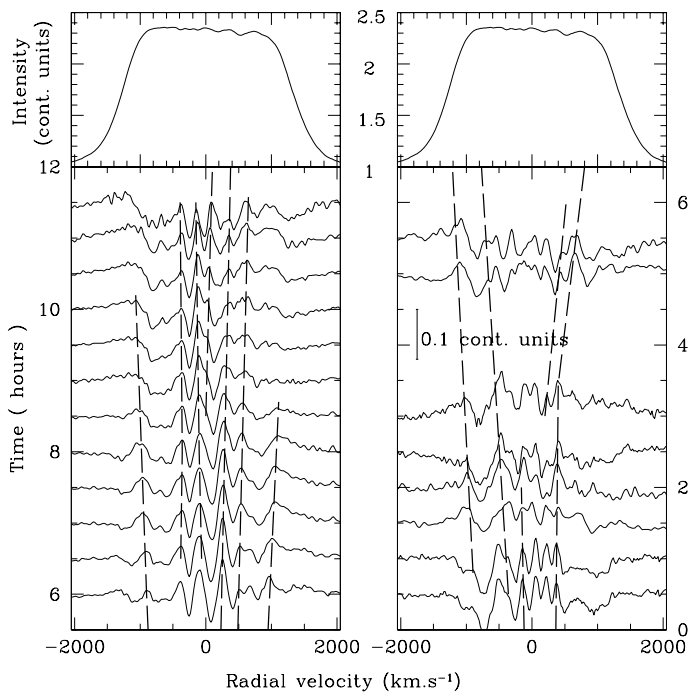


Figure 8. Clump evolution during two nights: left panel - 21/07/1999; right panel - 22/07/1999. The mean profile for all runs for the CIII $\lambda 5696$ line is shown in the upper panels. The bottom panels show montages of the deviations from the mean profile. In this plot we trace only the longest-living structures (straight dashed lines). However, practically all moving features were chosen for further analysis (Fig. 9).

periodic variations show coherent patterns in two regions separated by $\sim 50\text{\AA}$ (~ 250 resolution elements). We further discuss the 0.83 ± 0.04 d period in section 4.2.

3.2 Spectral-line variability

3.2.1 The β wind-velocity law

We then examined the rapid spectral variations in order to try and constrain the β wind-velocity law. To achieve this goal, the mean spectrum mentioned in section 3.1.2, was subtracted from the individual (unfiltered) spectra. Figure 8 displays examples of the spectral variability of the CIII $\lambda 5696$ emission line for the nights of July 21 and July 22, 1999. With the removal of the mean profile (top panels), it is much easier to follow relatively weak emission details travelling on top of the broadest lines (for similar results in other stars see Grosdidier et al. 2001; Lépine & Moffat 1999). As can be seen in Figure 8, individual subpeaks can be followed typically for several hours. It is customary to relate the small emission peaks to small-scale density enhancements (“clumps” or “blobs”) moving with the WR wind. Blobs are assumed to follow a β wind-velocity law like the rest of the wind (in fact they may constitute the wind as a whole):

$$v(r) = v_{\infty} \left(1 - \frac{R_{\star}}{r}\right)^{\beta}. \quad (2)$$

Their acceleration is

$$a(v) \equiv v \frac{dv(r)}{dr} = \beta \frac{v^2}{R_{\star}} \left[\left(\frac{v}{v_{\infty}}\right)^{-\frac{\beta}{2}} - \left(\frac{v}{v_{\infty}}\right)^{\frac{\beta}{2}} \right]^2. \quad (3)$$

The latter is equivalent for $\beta \gtrsim 2$ to (Lépine & Moffat 1999):

$$a(v) = [v \ln(\frac{v}{v_{\infty}})]^2 / \beta R_{\star}. \quad (4)$$

Assuming $v_{\infty} = 1885 \text{ km s}^{-1}$ and $R_{\star} = 4.5 R_{\odot}$ for WR137 (see Table 2) one can obtain an estimate of β .

Following individual subpeaks (Fig. 8), one can draw straight lines which have a slope proportional to the radial acceleration (i.e. the actual acceleration projected by an angle θ onto the line of sight) of the moving features. Thus, measured accelerations (a_R) along with the derived radial velocities (v_R) are plotted in an acceleration-velocity diagram (Fig. 9), which is traditionally used to constrain parameters of the β wind-velocity law. The RVs of the subpeaks have been measured by fitting gaussian profiles to the moving peaks, assuming $\sigma(RV) \sim 50 \text{ km s}^{-1}$ for the blobs in each spectrum. The least-square fitting of a straight line to the positions of the peaks provides estimates of the standard deviations for the acceleration. Due to the exceptional temporal coverage of the two nights represented in Figure 8, it was possible to follow subpeaks even in the regions corresponding to the steep flanks of the CIII $\lambda 5696$ line. These features move with greater radial acceleration than the blobs originating near the centre of the line, due to projection effects, i.e. one observes $a_R = a(v) \cos \theta$ and $v_R = v(r) \cos \theta$ at $\theta = \text{const.}$ for each subpeak, such that those at line centre have $\theta \simeq 90^\circ$, and those near line edge have $\theta \rightarrow 0^\circ$ on the blue side or $\theta \rightarrow 180^\circ$ on the red side.

Figure 9 shows that most of the components satisfy the expected $a_R v_R \geq 0$ relation, thus confirming the initial assumption that the moving peaks are related to radially accelerated structures leaving the star. Note that measurements with excessively large errors in acceleration, $\sigma_{a_R} \geq 0.02 \text{ km s}^{-2}$, have not been drawn in Figure 9 to avoid clutter. The 142 spectra (10 nights of observation at OHP, OMM, DAO, TO and RO during the period of 1999 July 21-31, except for July 29 when only one spectrum was available, plus 8 nights of observation at KPNO during the period of September 1999) result in $\beta R_{\star} = 25 \pm 5 R_{\odot}$, i.e. $\beta \simeq 5$, which is reasonably close to the range of values determined for WR137 by Lépine & Moffat (1999) ($\beta R_{\star} \sim 35-90 R_{\odot}$).

Note that the lower-acceleration structures outnumber the higher-acceleration ones. One may find an explanation for this in Figure 10, which shows the actual density of blobs compared to their theoretical density ($N(\Omega) \sim \sin(\theta)$), assuming constant spherically-symmetric density) versus the angle with respect to the line of sight (θ). The theoretical density maximum has been adjusted by a multiplicative factor to the maximum of the observed distribution. As can be seen, both observed and theoretical densities fall off as one goes away from $\theta=90^\circ$. However, there seems to be a real deficit in the observed density of blobs coming toward us ($\theta \sim 0^\circ$) or going away from us ($\theta \sim 180^\circ$) compared to the expected density. This can be explained by the fact that events responsible for the high acceleration structures normally occur far from the centre of the spectral line, thus being difficult to observe and track: (1) the corresponding features move rapidly and require good temporal coverage and (2) they are hard to recognize and trace because of their po-

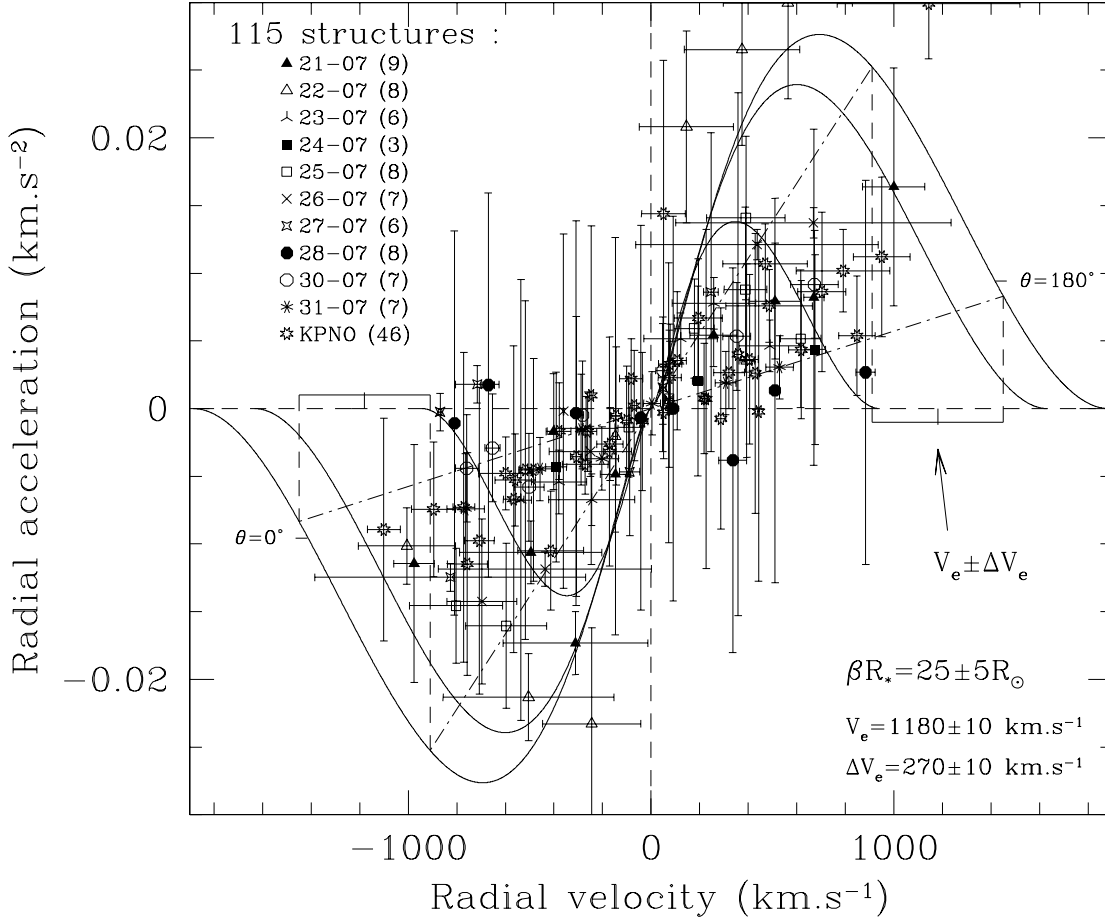


Figure 9. Radial acceleration versus radial velocity for detected blob trajectories from the DAO, OMM, OHP, RO, TO spectra of CIII 5696 for the period of July, 1999. The horizontal bars span the range of observed RVs while the vertical bars represent \pm the standard deviations for the fitted accelerations. A few points, due to measurement errors, fall into “forbidden” regions, i.e. on the back-side of the wind coming toward us and vice versa, providing wrong-sign accelerations. Curves based on eq. (4) represent angles to the line of sight from $\theta=0$ to 180 degrees in steps of 30 degrees, left to right, bottom to top. The dash-dotted lines represent the inner and outer limits of the *ler* in velocity ($V_e = 1180 \pm 10 \text{ km s}^{-1}$ and $\Delta V_e = 270 \pm 10 \text{ km s}^{-1}$ for the CIII $\lambda 5696$ line) calculated according to Lépine & Moffat (1999) for $\beta R_* \sim 25 R_\odot$. The two zones delimiting the *ler* in velocity space are indicated by horizontal bars.

Table 2. Stellar parameters of HD192641.

distance (kpc)	R_* (R_\odot)	β	v_∞ (km s^{-1})	M_{WR} (M_\odot)	M_O (M_\odot)	M_{WR}/M_O	P years	L_X (erg s^{-1})
1.82^a	4.5 ± 2.5^a	5.6 ± 1.2^b	1885^a	4.4 ± 1.5^b	20.0 ± 2.0^c	0.22 ± 0.07^b	13.05 ± 0.18^b	$0.25 \pm 0.14 \cdot 10^{32d}$

(a) Nugis & Lamers (2000), Koesterke & Hamann (1995), v_∞ close to 1900 km s^{-1} from van der Hucht (2001); (b) this paper; (c) Vacca et al. (1996), Gies (2003); (d) Pollock et al. (1995).

sitions and broader/flatter profiles superposed on the steep slopes of the line. In Figure 9, the limits of the CIII $\lambda 5696$ line emission region (*ler*) have been calculated according to Lépine & Moffat (1999). Note that some points are located well outside the central cluster of points in Figure 9, i.e. outside the *ler* in the “allowed” regions. These “outliers” might result from the superior temporal coverage provided by the more complete data from July 21 and 22 and some nights from the KPNO dataset. This may have allowed one to follow weak blobs on the steep flanks of the lines, with

stochastic errors putting the odd point outside the allowed area.

3.2.2 Cross-correlation Analysis

We now verify if the variable subpeak patterns in the different emission lines are similar. A visual examination of the spectroscopic time series (Figs. 2, 4) does suggest that the variability pattern in different lines may indeed be similar, i.e. that specific narrow subpeaks show up in each line, at the same position of the line profile, and at any given time. To

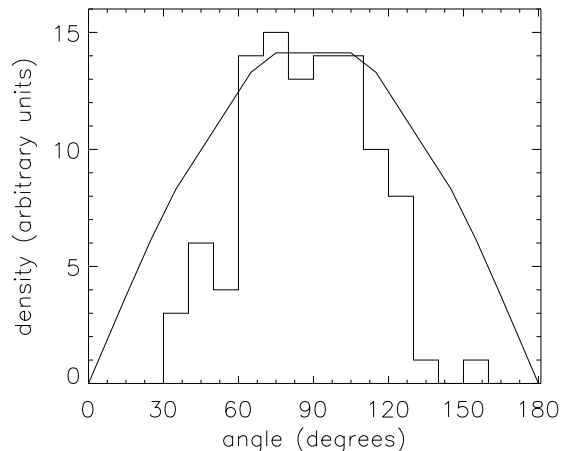


Figure 10. Actual density of blobs (histogram) compared to theoretical density (continuous line) versus angle of projection. See text for details. The relative deficit of observed blobs vs. theoretical number of fast structures towards the wings is likely due to the difficulty of measuring blobs in the wings of the CIII $\lambda 5696$ line.

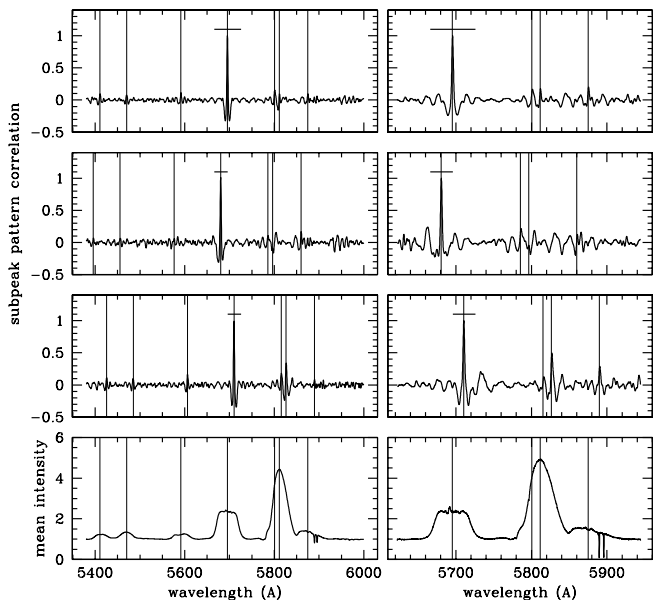


Figure 11. Results from the cross-correlation analysis of the variability patterns observed in the CIII $\lambda 5696$ emission line. The left panel shows the 1999 multi-site campaign (OHP, OMM, DAO, TO, RO) results while the right panel shows the results obtained for the KPNO run. Local maxima indicate regions where the variability patterns are correlated to those detected in CIII $\lambda 5696$ (note the value of 1.0 reached at 5696 Å indicating maximum correlation of the pattern with itself). Vertical lines mark positions of the most prominent emission lines relative to the part of CIII $\lambda 5696$ used for the correlation. Upper panels show the correlation functions calculated using the complete pattern in the CIII $\lambda 5696$ line ($5676 < \lambda < 5716$). The maxima are higher when one uses the patterns from the red side ($5696 < \lambda < 5716$) of the CIII line (bottom correlation panels). The correlation essentially vanishes when one uses the blue-side patterns, $5676 < \lambda < 5696$ (middle correlation panels).

quantify the similarity in the subpeak patterns, we apply the cross-correlation technique developed by Lépine et al. (2000). The well-defined variable subpeak pattern in the CIII $\lambda 5696$ line is used as a reference (the correlation response). Properly normalized, perfect match of the pattern at all times would yield a correlation value of 1.0, while the absence of any similarity should yield a correlation value close to 0.0, and -1.0 for an anti-correlation. Results are independent of the intensity of the pattern; hence if a pattern is identical to the reference pattern, it will yield a high correlation value, even if its amplitude is only a fraction of that of the reference pattern. One caveat is that instrumental noise can significantly degrade a subpeak pattern, especially if its intensity is low. Since the variable subpeak patterns in HeII $\lambda 5411$, CIV $\lambda 5471$ and OV $\lambda 5592$ are near the noise limit, one should not expect them to be highly correlated with CIII $\lambda 5696$. However, a small, but clear correlation should be regarded as significant.

In order to minimize the degradation in the correlation because of instrumental noise, we apply the cross-correlation technique to the wavelet-filtered spectroscopic time series (Figs. 2, 4). Results of the cross-correlation analysis are displayed in Figure 11. The cross-correlation is performed separately on the KPNO time series, compared to the multi-site (OHP, OMM, DAO, TO, RO) time series. As in Lépine et al. (2000), we use three different parts of the CIII $\lambda 5696$ line as the reference. First, we use the complete pattern in the CIII $\lambda 5696$ line ($5676 < \lambda < 5716$) as our correlation response (Fig. 11, top). As expected, we find a correlation value of 1.0 at the position of the CIII $\lambda 5696$ line itself. We also find secondary maxima *at the exact positions of all the most prominent emission lines*. Although some of these maxima are quite weak (with a correlation value of ≈ 0.1) they appear to be statistically significant because they occur at the exact wavelength positions expected for these atomic lines. The low correlation coefficient is a direct consequence of the weakness (proximity to the noise level) of the variability patterns in all the lines, except in CIII $\lambda 5696$. It is also possible that the variability patterns in the different lines are not exactly the same, as, generally, the lines do not form in the same parts of the wind.

We repeat the cross-correlation analysis, this time using only half of the variability pattern, either on the blue ($5676 < \lambda < 5696$) or red ($5696 < \lambda < 5716$) side of the CIII $\lambda 5696$ emission line (Fig. 11, second and third panels from the top). Results show a much stronger correlation when one uses the red side of the emission line. This perfectly mimics the behavior of the subpeaks in the presumably single star WR135 (Lépine et al. 2000). Most WR emission lines are flanked on their blue side by a weak *but variable* P-Cygni absorption trough, with a notable exception of the CIII $\lambda 5696$ emission line. Generally, the P-Cygni absorption trough is the most variable part of the profile. This may introduce an extra component of variability on the blue edge of the line. However, because CIII $\lambda 5696$ is unaffected by P-Cygni variations, the intrinsic variability of its blue edge is significantly different from that in the other lines. This explains the lower correlation between the blue edge of CIII $\lambda 5696$ and the blue edge of the other lines.

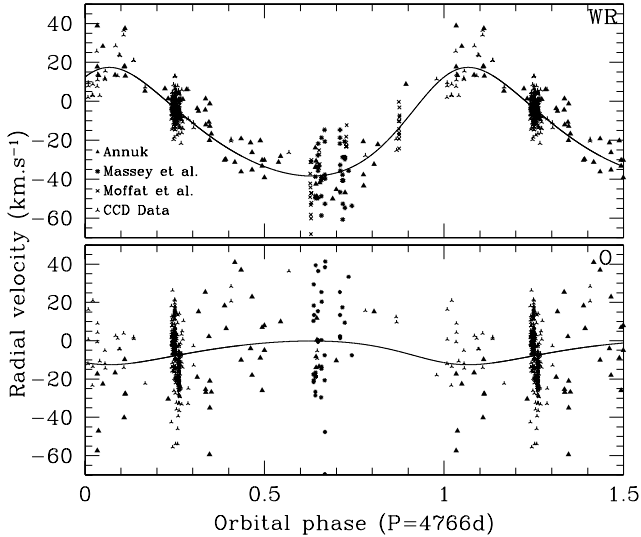


Figure 12. Radial velocities of the WR component phased with the 4766d orbit are shown in the upper panel: data from Annuk (1991, 1995), Massey et al. (1981) and Moffat et al. (1986) refer to photographic plates; the rest are measured from the current CCD spectra from DAO, OMM, OHP, RO, TO and KPNO. A typical standard deviation for the measurements is $\sim 15 \text{ km s}^{-1}$ for the former and 10 km s^{-1} for the latter. The bottom panel shows radial velocities for the O component. Full lines show the derived orbit.

3.3 Radial velocity variations: Orbit of the two components

Radial velocities (RV) were measured by fitting gaussian profiles to the HeI $\lambda 5876$ absorption line corresponding to the O star and cross-correlating the template (an average constructed from the data sets coming from different observatories) with the individual spectra in the region covering the strong CIV $\lambda\lambda 5802/12$ emission blend for the WR component. Typical uncertainty of the measurements run at $\sim 5 - 10 \text{ km s}^{-1}$ for an individual spectrum of the WR star and $\sim 10 - 20 \text{ km s}^{-1}$ for the O component. The results were corrected for systematic differences between observation sets. This adjustment was done taking the RO and OMM observations together, as in the overlapping epochs they show negligible relative shifts for the WR star measurements: the average velocity measured on the overlapping sub-sets (summer 1999) was $\langle V_{RO} \rangle = 3.0 \pm 6.7 \text{ km s}^{-1}$, $\langle V_{OMM} \rangle = 3.6 \pm 5.6 \text{ km s}^{-1}$. Then, we shifted the Kitt peak RV data into the RO and OMM system and applied the same procedure to the less numerous DAO and OHP sets (shifted relative to the RO+OMM system by $7 - 9 \text{ km s}^{-1}$). The Tartu set was not modified, as many of its data were taken later on, without any substantial overlap (see Table 3, published separately in the electronic version).

With the assumption that our data set alone may not be adequate in revealing the presumably long orbital period of WR137, we have incorporated earlier published RV measurements (Massey et al. 1981; Annuk 1991, 1995; Moffat et al. 1986). We applied the orbit-fitting algorithm from Bertiau & Grobbon (1969), assigning individual γ -velocities for the following sets: all the new CCD data for the WR component, as discussed above (made homogeneous by additional adjustments), then the WR sets of Massey et al.

Table 4. Orbital elements of HD192641

Parameter	WR	O
P (d)	4766 ± 66	
T_0 (JD)	2450198 ± 186	
ω ($^\circ$)	326 ± 15	
e	0.178 ± 0.042	
γ (km s^{-1})	-14.6 ± 0.9	-5.4 ± 0.7
K (km s^{-1})	27.9 ± 1.2	6.1 ± 1.3
$\sigma_{CCD}(o-c)$ (km s^{-1})	6	15
$\sigma_{plates}(o-c)$ (km s^{-1})	11	26
$a \sin i$ (AU)	12 ± 0.5	2.7 ± 0.6
$M \sin^3 i$ (M_\odot)	3.4 ± 1.0	15.3 ± 2.1

These parameters were derived with the combined radial velocities of CIV $\lambda 5806.0$ and absorption at HeI $\lambda 5875.6$ using the program developed by Bertiau & Grobbon (1969).

(1981) and Moffat et al. (1986) (photographic data, treated as 2 individual sub-sets), then 2 sets for the O star, one from our campaign, and the second described in Massey et al. (1981). This allowed us to compensate for the systematic differences in the RVs coming from different systems and epochs and evaluate the overall accuracy of the data: for the CCD data, σ_{o-c} is $\sim 6 \text{ km s}^{-1}$ for the orbital fit of the WR component while it is $\sim 15 \text{ km s}^{-1}$ for the O component, in line with the accuracies attained in measurements of individual spectra. The photographic plates yielded $\sigma_{o-c} \sim 11 \text{ km s}^{-1}$ and $\sim 26 \text{ km s}^{-1}$ for the WR and O components, respectively. Despite the different accuracy of the photographic and CCD data, we have kept the same weights while deriving orbital elements: less accurate photographic data have, nevertheless, an advantage of being taken at different epochs, while the CCD set mainly concentrates around 1998-2000, which is not very helpful in the situation when the orbital period exceeds 10 yrs.

The orbital elements obtained from the least-square fit of 427 WR RVs and 373 O RVs are listed in Table 4. Figure 12 shows that the computed orbit based on these parameters fits quite well all RV data obtained so far for the WR component. On the other hand, the fit for the O component is less precise, due to relatively large errors of the measurements.

4 DISCUSSION AND CONCLUSIONS

4.1 Spectral line variability

The presence of propagating stochastic structures indicates a clumpy wind as in all WR stars appropriately studied so far. Moreover, this study enabled us to constrain the parameters of the assumed β -law with good accuracy, due to the large quantity of data. We found $\beta R_* \simeq 25 \pm 5 R_\odot$ (according to Figure 9) which agrees marginally well with previous results, $\sim 35-90 R_\odot$ (Lépine & Moffat 1999), found using a wavelet analysis for WR137. However, one should be cautioned against any oversimplified interpretation of the β -law. Hamann et al. (2001) have discussed the apparent contradiction between the fast velocity law ($\beta \sim 1$) and the slow drift of the DACs (Discrete Absorption Components: Cranmer & Owocki 1996) in the winds of O stars. The explanation resides either in a difference between the velocity of patterns (DACs) and structures (modulations)

Table 3. Radial velocities of the WR and O components of WR137.

HJD- 2440000	RV $km\ s^{-1}$	HJD- 2440000	RV $km\ s^{-1}$	HJD- 2440000	RV $km\ s^{-1}$
WR		Comp.		$\sigma \sim 5-10\ km\ s^{-1}$	
KPNO	n=58	OHP	n=50	RO	n=67
11432.63091	0.2	10836.23647	21	11337.86891	-9.2
11432.66730	1.1	10837.24652	21	11350.80538	-5.1
11432.74425	3.5	10461.23148	15.54	11355.78767	-13.4
11432.76590	4.7	10454.24317	11.9	11364.71949	0.6
11432.78742	5.6	10456.22850	11.15	11364.84482	-11.1

Table 3 is published in its entirety in the electronic edition of this article. A portion is shown here for guidance regarding its form and content. n corresponds to the total number of spectra for one observatory.

in the wind or in different velocity laws co-existing at the same time in different spatial zones of the wind. Indeed, one may consider alternatives to the original β -law. E.g., Hillier & Miller (1999) introduced two power indices, thus dividing the wind into two distinct parts with different expansion laws. Although such a law might fit real data better, it is really no more physically justified than the simple β -law.

In addition, wavelet analysis and cross-correlation yield other interesting results. First, although weak, there is a correlation in variability patterns between all the most prominent lines in the $\lambda\lambda 5300 - 6000\ \text{\AA}$ range. Moreover, this correlation is stronger for the red-side than the blue-side variability patterns of CIII $\lambda 5696$: in the region of interest most emission lines -except the strong CIII $\lambda 5696$ line- show variable P-Cygni absorption troughs, which efficiently decorrelates the observed patterns. This behaviour was also detected in spectra of the single WC8 star WR135 (Lépine et al. 2000).

4.2 Short period

The $0.83d \pm 0.04d$ period could be related to large-scale, coherent structuring of the WR wind, taking the form of CIRs (Corotating Interaction Regions: Cranmer & Owocki 1996). CIRs are thought to be responsible for the periodic, $P=3.766d$, patterns re-appearing in the wind of WR6 (St-Louis et al. 1995, their Fig. 5), with a coherency timescale of at least ~ 4 rotation cycles.

If this 0.83d period was related directly to a phenomenon occurring on the surface of the star, it could imply a rotational velocity that is closer to the break-up velocity in WR137 than in WR6 or WR134. Taking parameters from Table 2, we obtain a rotational velocity of $275\ km\ s^{-1}$ and a break-up velocity of $475\ km\ s^{-1}$, which give $V_{rot}/V_{break-up} \simeq 0.58$. The results are not inconsistent with a rotational period, although one might also want to look for other explanations. This period could be only a fraction of the real rotation period, as is often supposed for CIRs (St-Louis et al. 1995) with multiple arms. Moreover, relatively rapid rotation of WR137 could be related to a flattened wind, as implied by the depolarized emission lines (Harries et al. 2000).

The O star companion with its period of 4766 days cannot possibly account for such short-term variability, as the 0.83d period is seen exclusively in the absorption troughs

of the lines originating in the WR wind. The existence of a much closer, low-mass compact companion could be another explanation. However, WR137 cannot be considered as a bright X-ray source: $L_X(0.2-2.4keV)=0.25 \pm 0.14\ 10^{32}\ erg\ s^{-1}$ (Pollock et al. 1995). On the other hand, the absence of a high X-ray output (compared to Cyg X-3 at $\sim 10^{38}\ ergs^{-1}$) does not necessarily mean that there is no compact companion (Ergma & Yungelson 1998; Marchenko et al. 1996) in so far as the *propeller* effect created by the rotating magnetic field may inhibit production of X-rays. A period of 0.83 days would imply an orbital separation $r_O \simeq 7\ R_\odot$ ($6.7 \pm 0.8\ R_\odot$) between the WR star and a hypothetical companion, according to the mass for the WR star (see Table 2) and considering a neutron star of $1.4\ M_\odot$. Since $R_* \simeq 4.5\ R_\odot$, this hypothesis remains plausible until further evidence can be found to the contrary.

Another possible source of the 0.83d variability could be related to pulsations of the WR star. Periods of radial pulsations in WR stars are predicted to range from several minutes to an hour (Bratschi & Blecha 1996) and thus can be ruled out. The same holds true for strange-mode pulsations (Saio et al. 1998), for which expected periods are more likely to be in the range of several minutes (Schaller 1992; Glatzel et al. 1993). The claim of $P \sim 627s$ for the southern Wolf-Rayet star WR40 (Blecha et al. 1992) was contradicted by the results of Marchenko et al. (1994) and Schneider et al. (1994), who claimed this period could be either spurious (caused by atmospheric transparency variations) or a pulsation appearing and vanishing on timescales of hours to a day (although no build-up or fading was noticed in the intensity of the variation). On the other hand, *non-radial* pulsations with a period ~ 20 hours (0.83d) are a possibility. They could be driven by the Eddington ϵ -mechanism (Maeder & Meynet 2002; Eddington 1918). The timescales of these modes would be of the order of hours to less than a day (Noels & Scuflaire 1986; Dziembowski 1994) so that they could be held accountable for the observed period in WR137. These are related to g+ modes of non radial pulsation, but are not believed to last more than a few 10^3 years. Further studies of WR137 with good temporal and spectral resolution (comparable to the current KPNO spectra) and high signal to noise ratio ($S/N \simeq 100-200$) could help to confirm and determine the origin of this small amplitude periodic variability. Note that the non-radial g-mode oscil-

lations should have a variable period (Balona et al. 1989), while the rotationally-modulated variability should provide a stable periodic modulation, thus providing means to distinguish between the two.

4.3 Orbital period and masses of the components

We have computed a reliable orbit for the WR star and provided the best possible estimate for the O-component orbit. Our derived period of 4766 ± 66 days is in perfect agreement with that found independently from the near-IR photometric data taken between 1985 and 1999 (Williams 2001), which yielded 4765 ± 50 days. The small eccentricity ($e = 0.178$) seems to be compatible with the episodic dust formation depicted in Marchenko et al. (1999), who assumed $e \leq 0.3$, based on the rather slow variability of the IR flux (Williams 2001) and behavior of the ejected dust cloud. Assuming that we see the system fairly near to edge-on, this would imply that the dust clumps observed in 1997 September - 1998 May with HST/NICMOS2 are indeed formed around the time when the O-companion was relatively close to the WR star. Indeed, the periastron passage seems to occur around 1996 (between February and October), according to Table 4. Assuming a distance to the system of 1.82 kpc (Table 2) and a spatial ejection velocity of $\sim 2000 \text{ km s}^{-1}$ (Marchenko et al. 1999), the displacement of the persistent dust cloud by $0.25''$ in May 1998 implies that the cloud was formed during periastron passage in 1996, long before the 1997-1998 images were taken. The diminishing orbital separation around periastron should intensify the wind-wind collision and, finally, increase the dust output (e.g. like another long-period dust-producing binary WR 140: Marchenko et al. (2003)). One more encouraging detail is the orientation of the WR orbit. Indeed, the behavior of the dust cloud implies that it was ejected from the system practically in the plane of the sky, at $\alpha_{dust} \sim 27^\circ$ relative to the plane (Marchenko et al. 1999). This fits well the longitude of periastron passage of the O star: $326^\circ - 180^\circ = 146^\circ$ (Table 4) which implies $\alpha_{orbit} = 180^\circ - 146^\circ = 34^\circ$, thus $\alpha_{orbit} \sim \alpha_{dust}$.

The van der Hucht (2001) catalogue provides an absolute magnitude of $M_V = -5.7$ for the WC7pd+O9 system, and $M_V = -4.52$ for the WR-component, implying $M_V = -5.25$ for the O-component. Thus, according to Vacca et al. (1996), the O9 component should have a spectral class between III and V and a mass of $M_O = 20 \pm 2 M_\odot$ (Gies 2003). This, in turn, implies $M_{WR} = 4.4 \pm 1.5 M_\odot$ and an inclination angle of $i = 67^\circ$. On the other hand, Nugis & Lamers (2000) give a mean of $M_{WR} = 13.4 \pm 1.3 M_\odot$ for WC7 stars which, if assumed to be applicable to the WC7 star in WR137, leads to $M_O = 60.9 \pm 15.5 M_\odot$ and $i = 39^\circ$. However, the shape of the ejected dust cloud strongly favors the larger value of inclination. Moreover, the mutual orientation of the orbital plane and the plane containing the flattened wind (Harries et al. 2000) also points to a rather high value of i .

ACKNOWLEDGMENTS

We wish to thank the Observatoire de Strasbourg for its support to LL's PhD thesis. AFJM thanks NSERC (Canada) and FQRNT (Québec) for financial support.

REFERENCES

- Annuk, K. 1991, in IAU Symp. 143, Wolf-Rayet Stars and Interrelations with Other Massive Stars in Galaxies, ed. K.A. van der Hucht & B. Hidayat (Dordrecht: Kluwer Academic Publishers), 245
- Annuk, K. 1995, in IAU Symp. 163: Wolf-Rayet stars: Binaries, colliding winds, evolution, ed. K.A. van der Hucht & P.M. Williams (Dordrecht: Kluwer Academic Publishers), 231
- Balona, L. A., Egan, J., & Marang, F. 1989, MNRAS, 240, 103
- Bertiau, F. C. & Grobben, J. 1969, *Ricerche Astronomiche*, 8, 1
- Blecha, A., Schaller, G., & Maeder, A. 1992, Nature, 360, 320
- Bratschi, P. & Blecha, A. 1996, A&A, 313, 537
- Conti, P. S. 2000, PASP, 112, 1413
- Cranmer, S. R. & Owocki, S. P. 1996, ApJ, 462, 469
- Dziembowski, W. A. 1994, in IAU Symp. 162: Pulsation, Rotation and Mass Loss in Early-Type Stars, ed. L.A. Balona, H.F. Henrichs & J.M. Le Contel (Dordrecht: Kluwer Academic Publishers), 55
- Eddington, A. S. 1918, MNRAS, 79, 2
- Ergma, E. & Yungelson, L. R. 1998, A&A, 333, 151
- Fullerton, A. W., Gies, D. R., & Bolton, C. T. 1996, ApJs, 103, 475
- Gies, D. R. 2003, IAU Symp. 212: A Massive Star Odyssey: From Main Sequence to Supernova, ed. K.A. van der Hucht, A. Herrero & E. César (San Francisco: Astronomical Society of the Pacific), 91
- Glatzel, W., Kiriakidis, M., & Fricke, K. J. 1993, MNRAS, 262, L7
- Grosdidier, Y., Acker, A., & Moffat, A. F. J. 2001, A&A, 370, 513
- Hamann, W.-R. 1991, in IAU Symp. 143: Wolf-Rayet Stars and Interrelations with Other Massive Stars in Galaxies, ed. K.A. van der Hucht & B. Hidayat (Dordrecht: Kluwer Academic Publishers), 81
- Hamann, W.-R. & Koesterke, L. 1998, A&A, 335, 1003
- Hamann, W.-R., Brown, J. C., Feldmeier, A., & Oskinova, L. M. 2001, A&A, 378, 946
- Harries, T. J., Hillier, D. J., & Howarth, I. D. 1998, MNRAS, 296, 1072
- Harries, T. J., Howarth, I. D., Schulte-Ladbeck, R. E., & Hillier, D. J. 1999, MNRAS, 302, 499
- Harries, T. J., Babler, B. L., & Fox, G. K. 2000, A&A, 361, 273
- Harries, T. J., Monnier, J. D., Symington, N. H., & Kurosawa, R. 2004, MNRAS, 350, 565
- Herald, J. E., Schulte-Ladbeck, R. E., Eenens, P. R. J., & Morris, P. 2000, ApJS, 126, 469
- Hillier, D. J. 1991, in IAU Symp. 143: Wolf-Rayet stars and interrelations with other massive stars in Galaxies, ed. K.A. van der Hucht & B. Hidayat (Dordrecht: Kluwer Academic Publishers), 59
- Hillier, D. J. & Miller, D. L. 1999, ApJ, 519, 354
- van der Hucht, K. A. 2001, New Astronomy Review, 45, 135
- Koesterke, L. & Hamann, W.-R. 1995, A&A, 299, 503
- Langer, N., Hamann, W.-R., Lennon, M., Najarro, F., Pauldrach, A. W. A., Puls, J. 1994, A&A, 290, 819

- Lépine, S. 1996, Wolf-Rayet stars in the framework of stellar evolution, ed. J.M. Vreux, A. Detal, D. Fraipont-Caro, E. Gosset & G. Rauw (Liege: Universite de Liege), 253
- Lépine S. & Moffat A. F. J. 1999, ApJ, 514, 909
- Lépine, S., Moffat, A.F.J., St-Louis, N., Marchenko, S.V., Dalton, M.J., Crowther, P.A., Smith, L.J., Willis, A.J., Antokhin, I.I. & Tovmassian, G.H. 2000, AJ, 120, 3201
- Maeder, A. & Meynet, G. 2002, In: Proceedings of the First Eddington Workshop on Stellar Structure and Habitable Planet Finding, ed. F. Favata, I. W. Roxburgh & D. Galadi (Noordwijk: ESA Publications Division), 49
- Marchenko, S. V., Antokhin, I. I., Bertrand, J., Lamontagne, R., Moffat, A. F. J., Piceno, A., & Matthews, J. M. 1994, AJ, 108, 678
- Marchenko, S. V., Moffat, A. F. J., Lamontagne, R., & Tovmassian, G. H. 1996, ApJ, 461, 386
- Marchenko, S. V., Moffat, A. F. J., Eversberg, T., Morel, T., Hill, G. M., Tovmassian, G. H., & Seggewiss, W. 1998, MNRAS, 294, 642
- Marchenko, S. V., Moffat, A. F. J., & Grosdidier, Y. 1999, ApJ, 522, 433
- Marchenko, S.V., Moffat, A.F.J., Vacca, W.D., Côté, S., & Doyon, R. 2002, ApJ, 565, L59
- Marchenko, S.V., Moffat, A.F.J., Ballereau, D., Chauville, J., Zorec, J., Hill, G.M., Annuk, K., Corral, L.J., Demers, H., Eenens, P.R.J., Panov, K.P., Seggewiss, W., Thomson, J.R. & Villar-Sbaffi, A. 2003, ApJ, 596, 1295
- Massey, P., Conti, P. S., & Niemela, V. S. 1981, ApJ, 246, 145
- Moffat, A. F. J., Lamontagne, R., Shara, M. M., & McAlister, H. A. 1986, AJ, 91, 1392
- Moffat, A. F. J., Drissen, L., Lamontagne, R., & Robert, C. 1988, ApJ, 334, 1038
- Monnier, J.D., Tuthill, P.G., & Danchi, W.C. 1999, ApJ, 525, L97
- Monnier, J.D., Tuthill, P.G., & Danchi, W.C. 2002, ApJ, 567, L137
- Morel, T., St-Louis, N., & Marchenko, S. V. 1997, ApJ, 482, 470
- Morel T., Marchenko, S.V., Eenens, P.R.J., Moffat, A.F.J., Koenigsberger, G., Antokhin, I.I., Eversberg, T., Tovmassian, G.H., Hill, G.M., Cardona, O. & St-Louis, N. 1999, ApJ, 518, 428
- Noels, A. & Scufflaire, R. 1986, A&A, 161, 125
- Nugis, T., Crowther, P. A., & Willis, A. J. 1998, A&A, 333, 956
- Nugis, T. & Lamers, H. J. G. L. M. 2000, A&A, 360, 227
- Panov, K. P., Altmann, M., & Seggewiss, W. 2000, A&A, 355, 607
- Pollock, A. M. T., Haberl, F., & Corcoran, M. F. 1995, in IAU Symp. 163: Wolf-Rayet stars: Binaries, colliding winds, evolution, ed. K.A. van der Hucht & P.M. Williams (Dordrecht: Kluwer Academic Publishers), 512
- Prinja, R. K., Fullerton, A. W., & Crowther, P. A. 1996, A&A, 311, 264
- Roberts, D. H., Lehar, J., & Dreher, J. W. 1987, AJ, 93, 968
- Saio, H., Baker, N.H., & Gautschy, A. 1998, MNRAS, 294, 622
- Scargle J. D. 1982, ApJ, 263, 835
- Schaller G. 1992, PhD. Thesis Univ. Genève
- Schneider, H., Kiriakidis, M., Weiss, W. W., Glatzel, W., & Fricke, K. J. 1994, in IAU Symp. 162: Pulsation, Rotation and Mass Loss in Early-Type Stars, ed. L.A. Balona, H.F. Henrichs & J.M. Le Contel (Dordrecht: Kluwer Academic Publishers), 53
- St-Louis, N., Dalton, M. J., Marchenko, S. V., Moffat, A. F. J., & Willis, A. J. 1995, ApJ, 452, 57
- Tuthill, P.G., Monnier, J.D., & Danchi, W.C. 1999, Nature, 398, 487
- Vacca, W. D., Garmany, C. D., & Shull, J. M. 1996, ApJ, 460, 914
- Williams, P. M., Longmore, A. J., van der Hucht, K. A., Talevera, A., Wamsteker, W. M., Abbott, D. C., & Tesesco, C. M. 1985, MNRAS, 215, 23P
- Williams, P.M. et al. 1995, in IAU Symp. 163: Wolf-Rayet stars: Binaries, colliding winds, evolution, ed. K.A. van der Hucht & P.M. Williams (Dordrecht: Kluwer Academic Publishers), 335
- Williams, P.M. et al. 2001, MNRAS, 324, 156

Table 3: Radial velocities of the WR and O components of WR137.

HJD- 2440000	RV km s ⁻¹	HJD- 2440000	RV km s ⁻¹	HJD- 2440000	RV km s ⁻¹
WR		$\sigma \sim 5-10 \text{ km s}^{-1}$			
Comp.					
KPNO	n=58	OHP	n=50	RO	n=67
11432.63091	0.2	10836.23647	21	11337.86891	-9.2
11432.66730	1.1	10837.24652	21	11350.80538	-5.1
11432.74425	3.5	10461.23148	15.54	11355.78767	-13.4
11432.76590	4.7	10454.24317	11.9	11364.71949	0.6
11432.78742	5.6	10456.22850	11.15	11364.84482	-11.1
11432.80894	4.6	11341.59419	-1.23	11365.80460	-5.2
11432.83074	4.2	11342.36760	1.559	11366.77194	8.6
11432.85236	5.0	11342.58567	-2.49	11367.77182	-19.7
11434.61284	-4.6	11343.36673	-3.6	11369.84141	-5.4
11434.63413	-4.7	11340.41103	-1.35	11370.79363	-7.2
11434.65526	-4.1	11343.59035	-3.5	11371.73009	-6.1
11434.67980	-3.8	11344.39733	-0.5	11375.77142	-18.5
11434.70112	-3.7	11344.58519	-4.4	11376.74935	-10.0
11434.72270	-5.4	11345.37261	-7	11376.80593	-2.7
11434.74391	-4.7	11345.50225	-2.9	11382.72132	0.0
11434.76517	-4.3	11345.59739	-3.6	11382.77903	-2.6
11434.78992	-4.1	11346.36895	-6.72	11385.70842	-11.9
11434.81113	-5.7	11346.59049	-4.89	11385.77623	-10.5
11434.83291	-5.7	11340.59252	-6.55	11385.84749	-14.6
11434.83291	-4.5	11341.36825	1.24	11387.63652	6.7
11435.67243	-5.1	11380.54582	-5.4	11387.75767	7.9
11435.69391	-5.5	11381.52224	-5.13	11389.79351	-0.4
11435.71503	-5.1	11381.53335	-5.8	11390.70328	-4.7
11435.73965	-4.2	11381.61599	-2.07	11390.84508	-5.2
11435.76085	-3.7	11381.62710	-2.5	11392.63117	-7.4
11435.78206	-3.5	11382.54170	-6.4	11392.74221	-5.8
11435.80327	-4.2	11382.55281	-6.7	11392.86702	-0.6
11435.82453	-5.7	11382.56392	-5.9	11393.62205	-3.0
11435.84564	-5.1	11382.58962	-5.8	11393.73725	-3.0
11435.86682	-4.2	11382.60490	-3.8	11393.84444	1.1
11436.69696	-7.3	11383.61162	-8.6	11394.65833	-6.4
11436.73337	-6.6	11384.51257	-9	11394.84712	0.5
11436.77404	-5.1	11384.55007	-11	11399.63261	3.8
11436.81340	-5.5	11384.62785	-7.2	11399.75451	4.8
11436.85282	-4.5	11385.36814	-4.7	11399.84941	5.3
11437.73179	-7.0	11385.39245	-4.8	11401.63055	-2.0
11437.75827	-6.8	11385.54453	-7.13	11401.76374	5.1

Table 3: Radial velocities of the WR and O components of WR137.

HJD- 2440000	RV km s ⁻¹	HJD- 2440000	RV km s ⁻¹	HJD- 2440000	RV km s ⁻¹
11437.79076	-7.7	11385.61120	-4.9	11406.66594	1.3
11437.82291	-7.5	11386.36955	-5.6	11408.61424	-0.1
11437.85480	-5.2	11386.39177	-6.458	11411.62466	-17.4
11437.88721	-2.9	11386.41608	-7.4	11411.74291	-4.8
11438.69784	-7.0	11386.43552	-7.06	11411.84996	-4.6
11438.73373	-4.9	11386.47441	-7.16	11412.63227	-7.0
11438.76977	-6.1	11386.49802	-7.47	11419.66042	7.9
11439.61786	-7.1	11386.52372	-6.8	11419.78342	0.3
11439.65384	-7.0	11386.54663	-6.8	11420.60184	-11.9
11439.68991	-7.8	11386.56399	-5.65	11420.64735	-8.4
11439.72551	-7.8	11386.58691	-5.23	11422.61497	-2.9
11439.79953	-6.7	11386.60011	-5.35	11425.68846	-4.2
11439.84255	-5.7	11386.62163	-4.5	11426.61086	-10.3
11439.88505	0.2			11427.59070	-7.2
11440.60758	-8.0			11436.58690	-16.6
11440.64339	-5.4			11437.71606	-6.6
11440.67904	-13.8			11438.67730	-5.5
11440.71249	-8.7			11439.57380	-6.5
11440.76056	-7.4			11440.67911	0.5
11440.79611	-8.3			11443.63837	-0.5
11440.83513	-8.6			11444.67690	-2.3
				11452.59047	-7.7
				11457.56869	-6.6
				11458.54508	0.3
				11459.58972	-5.2
				11463.58461	1.8
				11466.57143	-21.6
				11467.56092	-7.6
				11472.53462	-9.2
				11480.54107	-13.8
TO	n=27	DAO	n=41	OMM	n=53
11338.449160	1.522	6658.71105	-8.0	10705.66017	36.5
11344.441250	-2.938	7364.83470	-20.4	10703.50189	34
11406.391227	-6.8	7365.81336	-19.5	10094.45759	11.4
11428.306354	-11.499	8131.74716	-26.3	10230.83243	2
11428.327006	-9.131	8507.81626	-33.8	10234.66781	8
11428.395544	-7.193	8508.91342	-31.6	10234.81645	9.6
11430.356863	-8.594	9146.89239	-27.8	10288.83971	3.3
11431.295038	-0.509	9555.88207	-19.4	10293.76074	8.8

Table 3: Radial velocities of the WR and O components of WR137.

HJD- 2440000	RV km s ⁻¹	HJD- 2440000	RV km s ⁻¹	HJD- 2440000	RV km s ⁻¹
11431.377708	-5.153	9561.80083	-25.2	10293.86173	2.9
11431.388773	-2.956	10386.63950	2.9	10346.62576	25.7
11433.360139	-7.352	10624.89855	13.112	10352.50369	7.7
11437.272685	-3.652	10643.91800	23.9	10356.48554	11
11437.292211	-6.946	10655.88490	23.5	10357.49225	13.9
11437.303727	-1.16	11380.74616	2.5	10595.79001	28.5
11441.294398	-0.946	11380.79199	1.5	10989.63747	7.4
11441.541644	3.835	11380.83892	2.9	11348.66814	-8.4
11465.396447	-7.521	11380.87999	-9.079	11348.82453	-14.3
11474.261458	-16.188	11380.92240	-11.03	11349.58565	-1.4
11474.392431	5.916	11380.96395	-8.9	11349.82111	1.6
11475.407523	-9.714	11380.98503	-9	11350.59191	-6.9
11486.366365	-10.733	11381.72395	6.2	11350.82786	0.4
11489.331007	-14.037	11381.80548	1.234	11351.64046	4.7
11498.259381	-8.051	11381.89040	12.55	11351.81276	1.0
11559.253623	6.240	11381.97824	-6.1	11352.60560	3.4
11563.185521	-8.957	11382.71962	-6.6	11352.73782	-2.3
11630.538148	-10.972	11382.79005	-5	11353.58630	-6.0
11633.574381	-13.578	11382.86844	-8.3	11353.79974	2.5
		11384.78177	-8.3	11354.75562	4.7
		11384.80591	0.36	11356.60721	-3.6
		11384.82952	-4.5	11356.75787	-2.6
		11384.91245	-11.7	11360.59659	-6.6
		11384.95954	-11.3	11381.57328	-3.9
		11385.72851	4.7	11381.59887	-2.7
		11385.77583	-1.094	11381.73348	-7.0
		11385.85013	-9.6	11381.81508	-3.5
		11385.93224	-13.22	11382.59616	-2.0
		11385.97822	-13.09	11382.80272	-8.8
		11386.71702	2.61	11383.57108	-5.0
		11386.80722	13.05	11383.68687	3.2
		11386.89773	-8.5	11386.61144	-1.4
		11386.97767	-4.028	11386.62409	3.6
				11387.66687	-14.6
				11387.79825	-5.9
				11388.78837	-6.0
				11389.56339	-5.0
				11389.68728	-6.5
				11390.56831	-9.9

Table 3: Radial velocities of the WR and O components of WR137.

HJD- 2440000	RV km s ⁻¹	HJD- 2440000	RV km s ⁻¹	HJD- 2440000	RV km s ⁻¹
				11390.56354	-11.7
				11390.77701	-8.5
				11439.50374	-12.7
				11440.50850	-9.2
				11441.51545	-9.4
				11450.51896	-13.2
O		Comp.		$\sigma \sim 10\text{-}20 \text{ km s}^{-1}$	
KPNO	n=58	OHP	n=50	RO	n=67
11432.63091	-13.5185	10454.24317	-5.1	11337.86891	-42.5
11432.66730	-16.26092	10456.22850	-11.89	11350.80538	-6.37
11432.74425	-16.43353	10461.23148	-14.41	11355.78767	-55.45
11432.76590	-22.45189	10836.23647	1.9	11364.71949	3.65
11432.78742	-24.37468	10837.24652	1.01	11364.84482	-70.77
11432.80894	-21.93245	11340.41103	-1.85	11365.80460	-7.15
11432.83074	-18.91516	11340.59252	1.85	11366.77194	-6.8
11432.85236	-21.95645	11341.36825	-13.8	11367.77182	-13.32
11434.61284	-15.16735	11341.59419	4.22	11369.84141	12.83
11434.63413	-16.31576	11342.36760	3	11370.79363	-16.45
11434.65526	-6.662515	11342.58567	10.85	11371.73009	-26.07
11434.67980	-13.01406	11343.36673	-1.48	11375.77142	-14.77
11434.70112	-13.86969	11343.59035	1.48	11376.74935	-19.67
11434.72270	-7.824744	11344.39733	7.72	11376.80593	-6.4
11434.74391	-5.973826	11344.58519	2.94	11382.72132	-14.85
11434.76517	-10.5995	11345.37261	5.5	11382.77903	-9.55
11434.78992	-11.63463	11345.50225	9.46	11385.70842	-9.01
11434.81113	-13.46747	11345.59739	13.04	11385.77623	-6.34
11434.83291	-10.50864	11346.36895	0.0076	11385.84749	-3.11
11434.85406	-10.30561	11346.59049	2.63	11387.63652	-20.37
11435.67243	-26.20675	11380.54582	-4.41	11387.75767	6.92
11435.69391	-18.30422	11381.52224	13.2	11389.79351	-14.05
11435.71503	-22.35929	11381.53335	11.04	11390.70328	0.34
11435.73965	-18.4663	11381.61599	4.7	11390.84508	-27.5
11435.76085	-19.68067	11381.62710	1.53	11392.63117	-19.73
11435.78206	-22.65578	11382.54170	1.74	11392.74221	-8.7
11435.80327	-19.36417	11382.55281	16.32	11392.86702	-9.58
11435.82453	-21.50846	11382.56392	2.12	11393.62205	-22.02
11435.84564	-21.05155	11382.58962	11.6	11393.73725	-7.03
11435.86682	-15.50149	11382.60490	16.6	11393.84444	-0.02
11436.69696	-5.303081	11383.61162	-3.2	11394.65833	-53.78

Table 3: Radial velocities of the WR and O components of WR137.

HJD- 2440000	RV km s ⁻¹	HJD- 2440000	RV km s ⁻¹	HJD- 2440000	RV km s ⁻¹
11436.73337	-9.013728	11384.51257	2.8	11394.84712	-17.47
11436.77404	-9.866422	11384.55007	2.8	11399.63261	-6.83
11436.81340	-15.71549	11384.62785	21.15	11399.75451	-20.93
11436.85282	-11.06516	11385.36814	1.6	11399.84941	-5.23
11437.73179	-13.24795	11385.39245	0.19	11401.63055	-7.06
11437.75827	-12.6186	11385.54453	5.36	11401.76374	2.23
11437.79076	-13.47749	11385.61120	1.06	11406.66594	-32.28
11437.82291	-15.51589	11386.36955	4.1	11408.61424	0.89
11437.85480	-15.07061	11386.39177	1.74	11411.62466	-18.52
11437.88721	-11.87879	11386.41608	-4.36	11411.74291	-9.92
11438.69784	-6.320427	11386.43552	6.51	11411.84996	-2.96
11438.73373	-10.07528	11386.47441	-1.9	11412.63227	14.06
11438.76977	-13.90196	11386.49802	-3.96	11419.66042	9.32
11439.61786	-18.67389	11386.52372	-0.79	11419.78342	3.03
11439.65384	-21.69705	11386.62163	2.16	11426.61086	-22.36
11439.68991	-23.57302			11427.59070	-39.32
11440.60758	-25.41989			11436.58690	-8.82
11440.64339	-23.52954			11437.71606	-2.07
11440.67904	-32.82693			11438.67730	-20.20
11440.71249	-25.43613			11439.57380	-2.21
11440.76056	-20.92215			11440.67911	-22.5
11440.79611	-25.29399			11443.63837	14.20
11440.83513	-24.58265			11444.67690	-28.94
				11452.59047	-17.47
				11457.56869	-8.37
				11458.54508	-1.35
				11459.58972	-24.98
				11463.58461	-7.77
				11466.57143	-24.27
				11467.56092	-13.06
				11472.53462	3.2978
				11480.54107	5.06
TO	n=27	DAO	n=41	OMM	n=53
11338.449160	18.18	6658.71105	-11.7	10705.66017	-14.03
11344.44125	-1.46	7364.83470	20.7	10703.50189	3.91
11406.391227	-35.8	7365.81336	28.4	10094.45759	-17.89
11428.306354	-23.46	8131.74716	36.4	10230.83243	-12.03
11428.327006	-20.63	8507.81626	-5.2	10234.66781	0.65
11428.395544	-19.3	8508.91342	-9.3	10234.81645	16.4

Table 3: Radial velocities of the WR and O components of WR137.

HJD- 2440000	RV km s ⁻¹	HJD- 2440000	RV km s ⁻¹	HJD- 2440000	RV km s ⁻¹
11430.356863	-22.6	9146.89239	15.7	10288.83971	-23.3
11431.295038	-21.19	9555.88207	12.49	10293.76074	21.01
11431.377708	-18.58	9561.80083	9.66	10293.86173	-13.5
11431.388773	-24.53	10386.63950	-10.64	10346.62576	
11433.360139	-27.73	10624.89855	1.25	10352.50369	-0.64
11437.272685	-32.53	10643.91800	-4.28	10356.48554	9.13
11437.292211	-22.35	10655.88490	-4.33	10357.49225	4.33
11437.303727	-3.12	11380.74616	21.56	10595.79001	2.61
11441.294398	-36.55	11380.79199	2.79	10989.63747	-22.31
11441.541644	-11.16	11380.83892	8.7	11348.66814	-6.97
11465.396447	-7.16	11380.87999	-4.36	11348.82453	-11.57
11474.261458	-33.25	11380.92240	-3.9	11349.58565	-15.93
11474.392431	-6.611	11380.96395	2.17	11349.82111	7.94
11475.407523	-11.35	11380.98503	-9.8	11350.59191	-2.62
11486.366365	-13.92	11381.72395	19.6	11350.82786	-2.32
11489.331007	0.74	11381.80548	13.8	11351.64046	-2
11498.259381	10.38	11381.89040	4.7	11351.81276	-13.87
11559.253623	-32.8	11381.97824	-5.11	11352.60560	26.26
11563.185521	-24.85	11382.71962	15	11352.73782	0.32
11630.538148	-2.67	11382.79005	14.94	11353.58630	-0.82
11633.574381	-12.758	11382.86844	15.83	11353.79974	-0.39
		11384.78177	15.7	11354.75562	12.1
		11384.80591	1.9	11356.60721	-3.64
		11384.82952	0.887	11356.75787	-4.64
		11384.91245	7.1	11360.59659	4.36
		11384.95954	2.36	11381.57328	5.36
		11385.72851	17.5	11381.59887	-14.7
		11385.77583	-4.2	11381.73348	3.6
		11385.85013	-13.8	11381.81508	11.6
		11385.93224	-6.55	11382.59616	-5.73
		11385.97822	-16.04	11382.80272	6.48
		11386.71702	3.5	11383.57108	2.3
		11386.80722	14.6	11383.68687	18.17
		11386.89773	-1.3	11386.61144	3.2
		11386.97767	-13.6	11386.62409	3.8
				11387.66687	-13.3
				11387.79825	-2.4
				11388.78837	1.76
				11389.56339	-1.3

Table 3: Radial velocities of the WR and O components of WR137.

HJD- 2440000	RV km s ⁻¹	HJD- 2440000	RV km s ⁻¹	HJD- 2440000	RV km s ⁻¹
				11389.68728	3.9
				11390.56354	-18.89
				11390.56831	-2.54
				11390.77701	-2.9
				11439.50374	-17.49
				11440.50850	-20.14
				11441.51545	-28.43
				11450.51896	-29.33

This Table is the electronic version Table 3. **n** corresponds to the total number of spectra for one observatory.